Applied Surface Science 504 (2020) 144545

Contents lists available at ScienceDirect

Applied Surface Science

journal homepage: www.elsevier.com/locate/apsusc

Full Length Article

Tunable localized surface plasmon resonance by self-assembly of trimetallic and bimetallic alloy nanoparticles via Ag sublimation from Ag/Au/Pt tri-layers

Sundar Kunwar, Puran Pandey, Sanchaya Pandit, Mao Sui, Jihoon Lee*

Department of Electronic Engineering, College of Electronics and Information, Kwangwoon University, Nowon-gu, Seoul 01897, South Korea

ARTICLE INFO

Keywords:
Plasmonics
Nanoparticles
Solid-state dewetting
AgAuPt NPs

ABSTRACT

In this work, various configurations, size, density and composition of AgAuPt and AuPt alloy NPs are demonstrated via the solid-state dewetting (SSD) of Ag/Au/Pt tri-layers on the transparent c-plane sapphire (0001) and the corresponding LSPR characteristics are thoroughly investigated along with the FDTD simulation. The SSD is adapted to convert the sputtered Ag/Au/Pt tri-layers into the definite alloy NPs based on the diffusion, inter-diffusion and energy minimization process. The resulting AgAuPt and AuPt NPs demonstrate much stronger plasmonic characteristics as compared to their counterparts with the tunable LSPR bands in the UV and VIS regions along with the various plasmon resonance modes such as dipolar (DR), quadrupolar (QR), multipolar (MR) and higher order (HO). Furthermore, the Ag atom sublimation demonstrates a significant role in the dewetting process, which significantly alters the size, shape and composition of alloy NPs, giving a rise to the development of AuPt NPs. In specific, the LSPR response attenuates with the sublimation, however, as the AuPt NPs in this study are significantly improved in terms of composition and configuration, i.e. shape, size and spacing, the LSPR responses are much stronger and dynamic as compared to the pure Pt NPs on sapphire in the previous studies.

1. Introduction

In the last decade, owing to the stimulating photon interaction with the metallic nanostructures at diverse wavelengths, the nano-plasmonics has made a great advance in a wide range of practical applications such as energy [1], electronics [2], catalysis [3], photonics [4], sensors [5], biomedical [6] and storage devices [7]. The collective oscillation, excitation and resonance of electrons at the surface of metallic nanostructures by the incident photons produce various indispensable effects such as strong light absorption and scattering, strong electromagnetic field, high charge carrier density and hot electron-hole pairs [1]. For instance, the incorporation of Au nanorods into the Bi_2WO_3 nanosheets significantly enhanced the NIR light absorption, leading to the improved photocatalytic performance based on the LSPR of Au nanorods [8].

The characteristics of plasmonic metallic nanostructures can be engineered depending on the necessities and demands by the systematic control of shape, size, crystal structure, exposed facets and density of plasmonic nanostructures [9–12]. At the same time, the alloy NPs with two or more metallic elements can provide added flexibility in the LSPR property control [13–15]. Alloy nanostructures are useful as they can readily incorporate the advantages of individual NPs and at the same time can offer novel properties and multi-functionalities [16–18]. For instance, the Au-Pd bimetallic alloy NPs remarkably improved the catalytic activity in the visible region as compared to the monometallic Au NPs because of the plasmon mediated charge distribution from the Au sites to the Pd sites within the alloy NPs [19]. Generally, the monometallic Ag and Au NPs have been being widely perused in the various plasmonic applications due to their strong LSPR responses whereas the Pt NPs, which however demonstrate weaker LSPR response, are commonly utilized in the catalytic applications due to their strong catalytic response and chemical robustness. Meanwhile, it has been demonstrated that the formation of bimetallic or trimetallic materials of Ag, Au and Pt can significantly improve the electrocatalytic, photocatalytic and physicochemical properties for oxidation-reduction reactions [20,21]. In this regard, the controlled fabrication, exploration of growth kinetics and LSPR characteristics of alloy NPs consisting of Ag, Au and Pt can be of fundamental interests for the realization of improved performance as well as for understanding of nanostructure–LSPR relationships, which has not been reported to the date.

* Corresponding author.
E-mail address: jihoonlee@kw.ac.kr (J. Lee).

https://doi.org/10.1016/j.apsusc.2019.144545
Received 19 June 2019; Received in revised form 5 October 2019; Accepted 28 October 2019
Available online 06 November 2019
0169-4332/

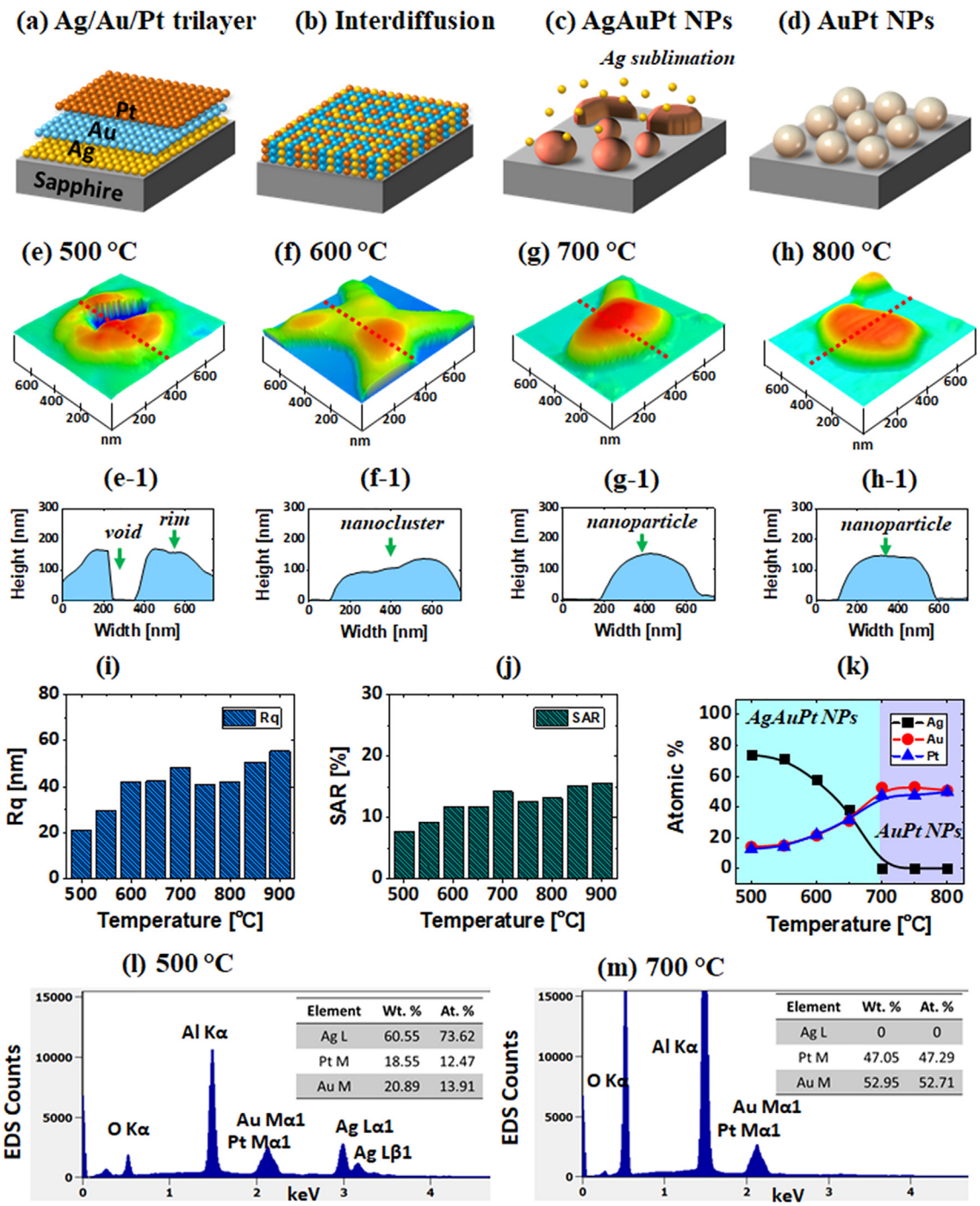

Fig. 1. Evolution of AgAuPt and AuPt alloy NPs by the dewetting of $Ag_{33nm}/Au_{9nm}/Pt_{9nm}$ tri-layers between 500 and 800 °C for 120 s. (a) – (d) Schematic of the fabrication of AgAuPt and AuPt alloy NPs. (e) – (h) Atomic force microscope (AFM) side-views of typical nanostructures at specific temperatures. (e-1) – (h-1) Corresponding line profiles. (i) – (j) Summary plots of RMS roughness (Rq) and surface area ratio (SAR). (k) Summary plots of atomic % of Ag, Au and Pt. (l) – (m) Energy dispersive x-ray spectroscope (EDS) spectra of AgAuPt and AuPt alloy at 500 and 700 °C.

In this paper, various configuration, size and density of AgAuPt and AuPt alloy NPs are demonstrated on c-plane sapphire (0001) along with their LSPR properties. The dynamic LSPR properties of these alloy NPs are characterized within the UV–Vis-NIR regions by the optical characterizations and finite difference time domain (FDTD) simulation. Specifically, the strong LSPR band in the visible region is commonly obtained for both AgAuPt and AuPt alloy NPs whose peak wavelength and bandwidth are varied based on the evolution of surface morphology and elemental composition of those alloy NPs. The solid-state dewetting of sputtered Ag/Au/Pt tri-layers is utilized to transform the uniform tri-layers into the definite alloyed NPs by means of the surface diffusion and interdiffusion of metallic atoms. The dewetting kinetics of the tri-layer film is controlled based on the variation of temperature, thickness and composition, which give rise to the small to large and the irregular to regular AgAuPt alloy NPs. Furthermore, the concurrent Ag atom sublimation changes the elemental composition in the AgAuPt NPs and thus the LSPR response and finally results in the formation of AuPt NPs at above 700 °C. In specific, the Ag/Au/Pt tri-layer of various thickness (3.4 nm ≤ n ≤ 51 nm) are annealed at various temperature, which give rise to the formation of densely packed tiny to the widely spaced large

AgAuPt (500 °C ≤ T ≤ 650 °C) and AuPt (700 °C ≤ T ≤ 800 °C) alloy NPs.

2. Experimental section

In this study, the double-side polished 430 μm thick *c*-place sapphire (0001) wafers with 0.1° off-axis were used to grow various AgAuPt and AuPt alloy nanostructures. Firstly, the large wafer was cleaved into the $6 \times 6\ mm^2$ square pieces by a mechanical saw. Then, the substrate was placed on a holder and subjected to a degassing process in a pulse laser deposition (PLD) chamber. The substrate degassing was performed at 600 °C for 30 min under 1×10^{-4} Torr that ensures the removal of oxides, particulates, trapped gaseous and water vapors from the sample. After degassing, the surface morphology and optical characteristics were examined as shown in Fig. S1. The surface morphology was quite smooth with the surface step height less than 0.4 nm. From the UV–VIS-NIR spectra measurement, a uniform response was obtained between 300 and 1100 nm with the average transmittance ~85% and reflectance ~13%.

Sequentially, various thickness of Ag, Au and Pt films were deposited on a clean sapphire (0001) sample by using a sputtering technique. The deposition of metal films was performed in a sputtering chamber under 1×10^{-1} torr. All metallic films were deposited at the fixed deposition rate of 0.05 nm/s (20 sec equals to 1 nm) and ionization current of 3 mA. Four different tri-layer sets were prepared to realize various shape, size and density of alloy NPs: $Ag_{33nm}/Au_{9nm}/Pt_{9nm}$, $Ag_{11nm}/Au_{3nm}/Pt_{3nm}$, $Ag_{5.5nm}/Au_{1.5nm}/Pt_{1.5nm}$ and $Ag_{2.2nm}/Au_{0.6nm}/Pt_{0.6nm}$. Subsequently, systematic annealing of samples was performed between 500 and 800 °C with the 50 °C interval and 120 s of annealing duration was equally allocated to each sample after reaching each target temperature. The overall annealing process was monitored and controlled by the computer recipe program for the consistency between samples. (For more details, please refer the sample deposition and fabrication in the supplementary information)

The surface morphology of as-fabricated alloy NPs was characterized by a non-contact mode atomic force microscope (NC-AFM) (XE-70, Park Systems Corp. South Korea) and scanning electron microscope (SEM) (CX-200, South Korea). For the elemental characterizations of the samples, energy dispersive x-ray spectroscopes (EDS) (Noran System 7, Thermo Fisher, United States and Ultimax, Oxford Instruments, United Kingdom) were utilized. The spatial resolution of EDS detector for elemental mapping is about 10 nm, which is integrated with the ultra-high resolution (0.7 nm) SEM (Regulus 8230, Hitachi, Japan). The elemental composition of alloy NPs in terms of atomic (at %) and weight (wt %) percentages were extracted from the EDS spectra acquired at 2 K magnification with ~ 12 mm working distance and 10 kV acceleration voltage. The detection limit of the EDS system was ~0.1 wt%. Optical characterization of as-fabricated trimetallic NPs was conducted by using a NOST system (Nostoptiks, South Korea), equipped with an ANDOR sr-500i spectrograph, CCD detector and various optical components. The electromagnetic (EM) field of as-fabricated NPs on sapphire was simulated by using a finite-difference time domain (FDTD) software (Lumerical Solutions, Canada). For simulation, the 3D AFM surfaces of typical NPs were imported into the structure space to incorporate the real NP morphologies. The complex refractive index was taken from the Palik's model for sapphire and Pt [22]. Similarly, for Au and Ag, the Rakic and CRC models were referenced respectively [23,24]. For the bimetallic and trimetallic alloy compositions, the dielectric constants were averaged from the pure metals based on the atomic % ratio [25,26]. (For more details, please refer the supplementary information).

3. Results and discussion

Fig. 1 shows the evolution of AgAuPt and AuPt alloy nanostructures by the annealing of $Ag_{33nm}/Au_{9nm}/Pt_{9nm}$ tri-layers between 500 and 800 °C for 120 s. Various evolution stages were observed along with temperature control: such as void formation, void and grain growth, nanocluster growth and nanocluster fragmentation. The Ag/Au/Pt tri-layers were annealed well below the melting point of all three constituent metals. Therefore, the overall transformation of quasi-continuous Ag/Au/Pt tri-layers into the isolated NPs can occur based on the solid-state dewetting mechanism [27,28]. Generally, the thin films deposited in an ambient temperature are metastable or unstable and will dewet or coalesce into the small particles when sufficient thermal energy beyond the activation energy of atoms is provided. This process can be firstly initiated by the atomic diffusion of atoms to the low energy sites in order to attain the surface energy equilibrium [29]. Depending upon the diffusivity of metals, various surface nanostructures of pure Ag [29], Au [30] and Pt [31] have been previously demonstrated on sapphire (0001) under various growth conditions. For instance, while Pt films showed minor surface roughness evolution without the formation of specific nanostructures up to 600 °C, the Ag and Au films already formed the well-developed semi-spherical NPs at ~400 °C due to the much higher diffusivity of Ag and Au atoms as compared to the Pt atoms [30–32].

In this study, the Ag, Au and Pt layers were deposited in a sequence depending upon the high surface diffusivity, low surface energy and low interaction force with sapphire [33]. In the Ag/Au/Pt configurations as shown in Fig. 1(a), the diffusivity reduces to the top layer direction whereas the surface energy increases. This may facilitate the overall dewetting process of Ag/Au/Pt tri-layers as the film adhered on substrate play major role in the growth kinetics [34,35]. The difference in the lattice constant, interdiffusion coefficient and interfacial energy with the multi-metallic layers could induce a complex dewetting process as compared with the monometallic layer dewetting. Initially, annealing of the Ag/Au/Pt tri-layers could lead to the interdiffusion of Ag, Au and Pt atoms into the other layers through the vacancies, grains boundaries and pinholes [36,37]. Along with the increased temperature of the system, the interdiffusion between Ag, Au and Pt atoms can be enhanced, which can increase the intermixed region further [38]. Thus, finally, each of the Ag, Au, Pt layers can be consumed by the formation of intermixed or alloyed layers as displayed in Fig. 1(b). Meanwhile, some asymmetry in the intermixing between the Ag, Au and Pt layer can be expected due to the difference in the diffusivity of Ag, Au and Pt atoms. Along with the enhanced surface diffusion and interdiffusion of different metallic atoms, the nucleation of voids could occur at low energy sites such as steps and grain boundaries, which initiates the dewetting process. With the increasing temperature, the diffusing atoms detach from the substrate allowing the voids to grow larger and forming rims around the voids [39]. This can result in the evolution of the three-dimensional nanoclusters as presented in Fig. 1(c) based on the Volmer-weber growth model owing to the stronger bonding energy between the metallic atoms than the metal and sapphire atoms [40].

On the other hand, the overall dewetting process and evolution of surface nanostructures can be affected by the concurrent sublimation of Ag atoms at increased temperature. This is due to the high vapor pressure of Ag atoms and the rate of sublimation exponentially increases with temperature, which eventually results in the AuPt alloy NPs as shown in Fig. 1(d). In this work, the dewetting of $Ag_{33nm}/Au_{9nm}/Pt_{9nm}$ tri-layer was initiated at 500 °C with the formation of voids more than 100 nm width as shown by the AFM image in Fig. 1(a). The large-scale surface morphologies and line profiles are provided in supplementary Figs. S2–S4. It was clearly observed that the void edges were grown more rapidly forming rims around them as the atomic diffusion through the edges can be much faster [29]. The corresponding line-profile of typical void-rim structure in Fig. 1(e-1) shows the rim height of ~180 nm. When the temperature was increased up to 600 °C, the size and number of voids were increased due to the coalescence with the neighboring ones and evolution of new nucleation sites [41,42]. Consequently, the network-like AgAuPt alloy nanoclusters were evolved as observed in Fig. 1(f). It was also observed that the local width of larger

nanoclusters varied, forming the neck-like structures, which can be due to the fluctuation of surface energy distribution. The growth of voids and nanoclusters at increasing temperature can be driven by the surface and interface energy minimization.

The evolution of surface morphology was further studied by the RMS roughness (Rq) and surface area ratio (SAR) in Fig. 1(i) and (j) respectively. The Rq quantify the average of surface profile height (y_i) as given by the relation: $R_q = \sqrt{\frac{1}{n}\sum_{i=1}^{n} y_i^2}$. Whereas the SAR provides the increment in the 3D surface area of NPs (A_{NP}) with respect to the 2D geometric area (A_s) of a substrate as expressed in the equation: $SAR = \frac{A_s - A_{NP}}{A_s} \times 100\%$. Generally, the Rq can be more closely related to the height modulation and the SAR can be more significantly affected by the density change while both the size and density can affect as seen in the equations. Both the Rq and SAR were gradually increased from ~20 nm to 60 nm and 8 to 18% along with the evolution of voids and connected nanoclusters between 500 and 650 °C indicating the increased height and surface area of the nanoclusters. In addition to the diffusion induced dewetting process, the Ag atomic sublimation also concurrently affected the voids growth and nanocluster formation [43]. The elemental ratio of AgAuPt trimetallic NPs was analyzed by the EDS spectra as shown in Fig. 1(k)–(m). The EDS spectra showed the presence of O, Al, Au, Pt and Ag peaks in each sample, in which O and Al are associated with the substrate and the Ag, Au and Pt are associated with the alloy nanostructures. The at % of Ag, Au and Pt peaks are summarized with respect to temperature in Fig. 1(k), which clearly indicates the significant alteration in the overall at % of elements. In specific, the Ag at % was gradually reduced between 500 and 650 °C and became zero at above 700 °C, indicating the complete sublimation loss of Ag atoms. The EDS spectra in Fig. 1(l) and (m) clearly showed the Au Mα1, Pt Mα1, Ag Lα1 and Ag Lβ1 peaks at 500 °C while only Au Mα1 and Pt Mα1 were depicted at 700 °C. In addition, the elemental distribution of dewetted nanostructures was investigated by the high-resolution SEM and EDS mapping as displayed in Fig. 2 and Figs. S5–S6. For the AgAuPt alloy nanoclusters fabricated at 600 °C, the SEM image and EDS phase maps of Ag, Au and Pt matched well as seen in Fig. 2(b)–(e). In the nanocluster region, the Ag, Au and Pt elements were found to be bright and uniform. Furthermore, the elemental line profile was extracted through the nanocluster as shown in Fig. 2(g)–(h), which clearly show the uniform distribution of Ag, Au and Pt elements in the NP clusters. This confirms that the Ag, Au and Pt atoms were well-intermixed along with the dewetting of the isolated alloy NPs.

Along with the further dewetting and sublimation of Ag atoms, the surface morphology of alloy nanocluster was drastically transformed at 700 °C as the network-like nanoclusters started to break down into the isolated NPs as seen in Fig. 1(g), which can be correlated to the Rayleigh-like instability of the large irregular nanoclusters [44]. The fragmentation of AgAuPt NP clusters continued up to 800 °C while those isolated already became the spherical from the irregular shape as shown in Fig. 1(h). The isolated NPs attained spherical shape as guided by the surface energy minimization and isotropic energy distribution, which can be ascribed to the process of gaining the equilibrium configuration and becoming thermally stable [45]. The typical spherical AuPt NPs had an average diameter (AD) and height (AH) of ~500 nm and 100 nm respectively as shown in Fig. 1(h-1). From the EDS analysis of the samples annealed above 700 °C, the Ag peaks were not detected, i.e. equal to the background signal (~180 EDS counts), due to the complete desorption by the sublimation of Ag atoms. Therefore, the NPs above 700 °C were the AuPt alloy and the at % of Au and Pt was found to be consistent as shown in the Fig. 1(k) and S4. To investigate the elemental distribution of AuPt alloy NPs after the Ag sublimation, a detailed elemental mapping analysis was performed with the sample annealed at 800 °C as shown in Fig. 2(i)–(p). As clearly seen in Fig. 2(j)–(m), the elemental maps of Au and Pt were intense and matched well with each other while the Ag map was negligible or the same as the background signal intensity. The background signal can be detected regardless of the choice of element. Further, the EDS line profile was extracted through the typical NP as shown in Fig. 2(o)–(p), which clearly show the high counts for Au and Pt while the Ag count was the same as the background, i.e. the detection limit of instrument. This again clearly signifies the complete sublimation of Ag atoms and formation of AuPt alloy NPs. From the morphological and elemental analysis of the samples at different temperatures, the overall evolution of alloy NPs was significantly affected by the atomic sublimation of Ag atoms along with the dewetting [44].

Fig. 3 presents the optical properties of various AgAuPt and AuPt NPs fabricated with the $Ag_{33nm}/Au_{9nm}/Pt_{9nm}$ tri-layers on sapphire (0001). Apparently, the optical properties of these alloy NPs were greatly affected by the evolution of surface morphologies and elemental compositions. The extinction, reflectance and transmittance spectra and corresponding normalized spectra are presented to show the various LSPR characteristics of AgAuPt and AuPt alloy NPs. In addition, the local e-field distributions on the typical alloy NPs were probed by the finite difference time domain (FDTD) simulation. To begin with, the optical spectra exhibited a two-grouped response and thus were divided into the two sections depending upon the elemental composition of the alloy NPs: i.e. the AgAuPt NPs below 650 °C in Fig. 3(a) – (c) and AuPt NPs above 700 °C in Fig. 3(a-1)–(c-1). In the case of the large AgAuPt nanoclusters, two pronounced LSPR bands were exhibited: one in the UV and the other in the VIS region as displayed in Fig. 3(a). The LSPR band can be assigned to the multipolar resonance (MR) mode in the VIS and higher order (HO) resonance mode in UV region respectively [46] as the average size of these nanoclusters was larger than 400 nm. The LSPR peaks were very strong with the large AgAuPt alloy nanoclusters at 500 °C and then gradually attenuated and broadened at increased temperature as shown in the normalized plot in Fig. 3(a-2). The reduction of LSPR intensity can be correlated to the sublimation of Ag atoms and overall size reduction of the AgAuPt alloy nanoclusters [47]. The e-field distributions of typical AgAuPt alloy NP at 470 nm corresponding to the MR mode is shown in Fig. 3(d)–(e). As the NPs was randomly structured, the e-field enhancement was much stronger at the sharp boundaries as clearly seen from the e-field profiles in the xy-plane. In the case of AuPt NPs above 700 °C, the LSPR intensity was further attenuated and broadened as shown in Fig. 3(a-1) and (a-3). Furthermore, the local e-field enhancement at the resonance wavelength in the VIS region also exhibited the reduced intensity as shown in Fig. 3(f)–(g). As the shape of NPs and transformed towards the spherical with the slight reduction in size, the UV and VIS were blue shifted to 320 and 460 nm. At the same time, the VIS resonance peaks were generally broadened as shown in Fig. 3(a-4) as the AgAuPt nanoclusters were evolved into the AuPt NPs after Ag sublimation.

In addition, Fig. 3(b) and (b-1) present the reflectance spectra of the AgAuPt and AuPt alloy NPs, which generally exhibited a narrow dip in the UV region at ~300 nm, a wide dip in the VIS region at the similar wavelength of extinction peaks. The dips in the reflectance spectra can be correlated to the absorption of light due to the various LSPR effect as discussed [46]. The reflectance dips were weakened and broadened with temperature, which can be correlated to the Ag sublimation at higher temperature. Furthermore, as the average size of AgAuPt alloy nanoclusters was decreased, the backscattering can be enhanced whereas the absorption can be decreased [48]. With the formation of AuPt NPs, the reflectance dips in the UV and VIS region were minorly reduced as displayed in Fig. 3(b-1) between 700 and 800 °C, which denotes the weaker LSPR with the AuPt NPs than the AgAuPt NPs. In the case of transmittance spectra in Fig. 3(c) and (c-1), both the AgAuPt and AuPt did not show obvious peak or dip formation. This can be caused by the high forward scattering of the large size NPs [49].

Fig. 4 shows the fabrication of medium size and moderate areal density of AgAuPt and AuPt alloy NPs with the $Ag_{11nm}/Au_{3nm}/Pt_{3nm}$ tri-layers between 500 and 800 °C for 120 s. The large-scale AFM images and corresponding line profiles are provided in Fig. S7. In this set, the overall film thickness (17 nm) was reduced by three times from the

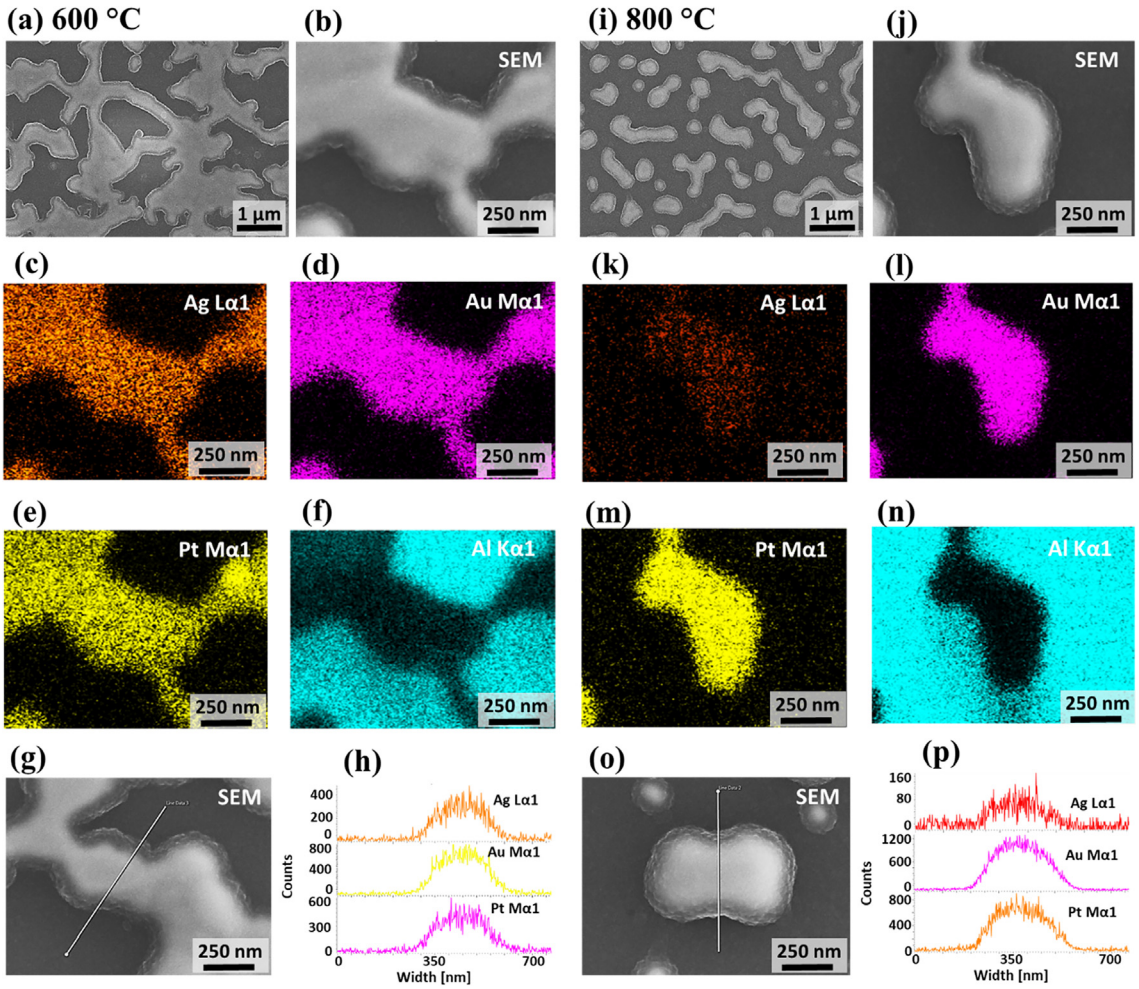

Fig. 2. Elemental analysis of the AgAuPt and AuPt alloy NPs fabricated with the $Ag_{33nm}/Au_{9nm}/Pt_{9nm}$ tri-layers at 600 and 800 °C for 120 s. (a) – (b) SEM images of the AgAuPt alloy nanoclusters at 600 °C. (c) – (f) Elemental maps of Ag, Au, Pt and Al. (g) – (h) SEM image and corresponding EDS line profile of AgAuPt alloy nanoclusters. (i) – (j) SEM images of AuPt alloy NPs at 800 °C. (k) – (n) Elemental maps of AuPt alloy NPs. The Ag map equlivalent to the background intensity clearly indicates the sublimation of Ag atoms from alloy NPs. (o) – (p) Typical AuPt alloy NP and the EDS line profile. The elemental map and line profile of Ag at 800 °C are within the detection limit of instrument indicating the absence of Ag atoms in the AuPt alloy NPs.

previous set and thus the resulting NPs were smaller, denser and more regular as seen in the AFM images. The dewetting degree directly depends on the initial film thickness and thus the resulting shape, size and density of NPs can vary largely even under the similar growth condition [50]. Generally, thinner films produce densely packed smaller NPs because of the rapid void nucleation, growth fragmentation of nanoclusters [51]. Furthermore, in the case of thinner Ag/Au/Pt tri-layers, the completion of interdiffusion between layers can be faster with the thinner individual layer. Therefore, by reducing the individual thickness of films the overall dewetting process was significantly enhanced, which resulted in the formation of isolated and spherical AgAuPt NPs even at lower annealing temperature. For instance, the irregular AgAuPt NPs of AD ~ 250 nm and AH ~ 70 nm were obtained even at 500 °C as seen in Fig. 4(a) and (a-1). These irregular NPs were gradually isolated and became more regular up to 600 °C along with the enhanced surface diffusion of atoms. The Rq and SAR were also mildly increased in this temperature range as the evolution of irregular to spherical AgAuPt NPs occurred.

Along with the enhanced agglomeration of atoms, the NP size is expected to increase, however, due to the simultaneous Ag sublimation the average size was not increased much. At the same time, the shape transformation of NPs was found to occur more rapidly due to the enhanced dewetting and Ag sublimation with temperature. The elemental analysis of these samples confirmed the accelerated sublimation of Ag atoms between 500 and 650 °C as shown in Fig. 4(g)–(i). Since the overall thickness of Ag/Au/Pt layers was decreased from the previous set, the dewetting and Ag atom sublimation occurred rapidly. Thus, much more isolated and semi-spherical AuPt NPs were formed at 650 °C, which occurred at a lower temperature from the previous set. Further increase in temperature resulted in the fragmentation of large NPs due to the Rayleigh-like instability and surface free energy minimization as discussed [45]. For instance, the NPs were widely isolated and relatively smaller at 700 °C as shown in Fig. 4(c). When the temperature was increased up to 800 °C, the areal density was gradually reduced whereas the vertical size tended to be increased. This can be correlated to the coalescence growth of the NPs as the smaller NPs can be merged to the larger ones in order to reach the lower chemical potential. In particular, the AH of NPs was between 48 and 52 nm whereas the AD was ~200 nm. Furthermore, the Rq and SAR also showed a mild increase with temperature as the size of NPs was minorly increased. The uniformity of NPs was also improved along with the enhanced dewetting at higher temperature as denoted by the reduced size of the Fourier filter transform (FFT) patterns. The elemental analysis of high temperature samples as shown in Fig. 4(g), (i) and S8 clearly demonstrate the evolution AuPt alloy NPs due to the Ag sublimation.

Fig. 5 presents the optical properties of medium-sized AgAuPt and AuPt alloy NPs fabricated with the $Ag_{11nm}/Au_{3nm}/Pt_{3nm}$ tri-layers. The alloy NPs in this set had AD of 200–250 nm and AH of 50–70 nm. As

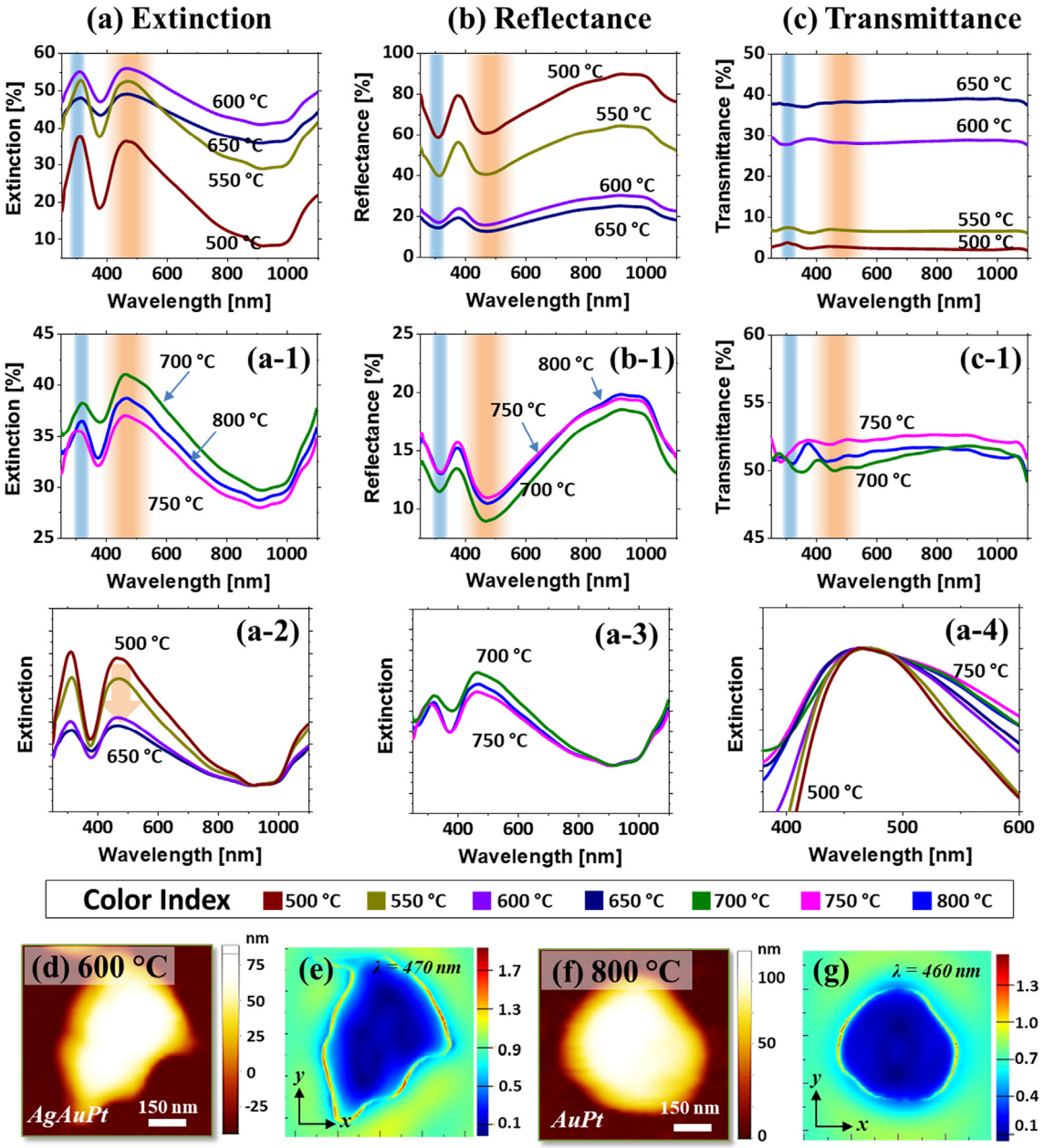

Fig. 3. Optical characteristics of various AgAuPt and AuPt alloy NPs on sapphire (0001) fabricated with the $Ag_{33nm}/Au_{9nm}/Pt_{9nm}$ tri-layers. (a) – (c) and (a-1) – (c-1) Extinction, reflectance and transmittance spectra of the AgAuPt and AuPt alloy nanostructures respectively. (a-2) – (a-4) Normalized extinction spectra. (d) and (f) AFM images of the typical alloy NPs chosen for the finite difference time domain (FDTD) simulations. (e) and (g) E-field intensity maps in x-y plane (top-view) of AgAuPt and AuPt NPs at a different wavelength as labeled.

compared to the previous set, these NPs were much smaller and denser, which induced the distinct LSPR responses as presented by the optical spectra. From the extinction spectra in Fig. 5(a) and (a-1), the AgAuPt NPs showed the LSPR peaks in the UV and VIS regions corresponding to the HR and MR modes [46]. The LSPR absorption peaks with the AgAuPt alloy NPs at 500 and 600 °C were found to be weaker than the large AgAuPt nanoclusters in the previous set, which can be correlated to the size of NPs and Ag content. However, interestingly between 500 and 600 °C, the LSPR intensity was similar although the Ag was sublimated with temperature [47]. This can be caused by the simultaneous effect of mild increment in NP size in Fig. 4(a)–(b) and the Ag sublimation within this temperature range.

In the case of AuPt alloy NPs above 650 °C, the broad peak in the VIS and minor peak in the UV region were observed. The MR resonance in the VIS region was slightly enhanced with temperature as shown in Fig. 5(a-2), which can be due to the minor size increment of the AuPt alloy NPs. Meanwhile, along with the improved uniformity of the AuPt alloy NPs at higher temperature, the MR band became slightly narrower as shown in Fig. 5(a-3). The e-field profiles of the typical AuPt alloy NPs are presented in Figs. 5(d)–(f) and S9, which showed the strong lobe on both sides of NPs, indicating the localized e-fields at ~300 and 490 nm corresponding to the HO and MR modes respectively. The e-field at VIS was slightly stronger than the one at UV, which agreed well with the experimental result. In the case of reflectance spectra, the AgAuPt NPs showed a UV dip at ~300 nm and a VIS dip at ~480 nm up to 600 °C as shown in Fig. 5(b) and (b-1). Although the overall size of NPs was increased, the absorption dips were slightly decreased with temperature as shown in Fig. 5(b-1), which can be correlated to the Ag sublimation from the NPs. With the formation of slightly smaller AuPt NPs above 650 °C, the reflectance dips were further attenuated, which can be due

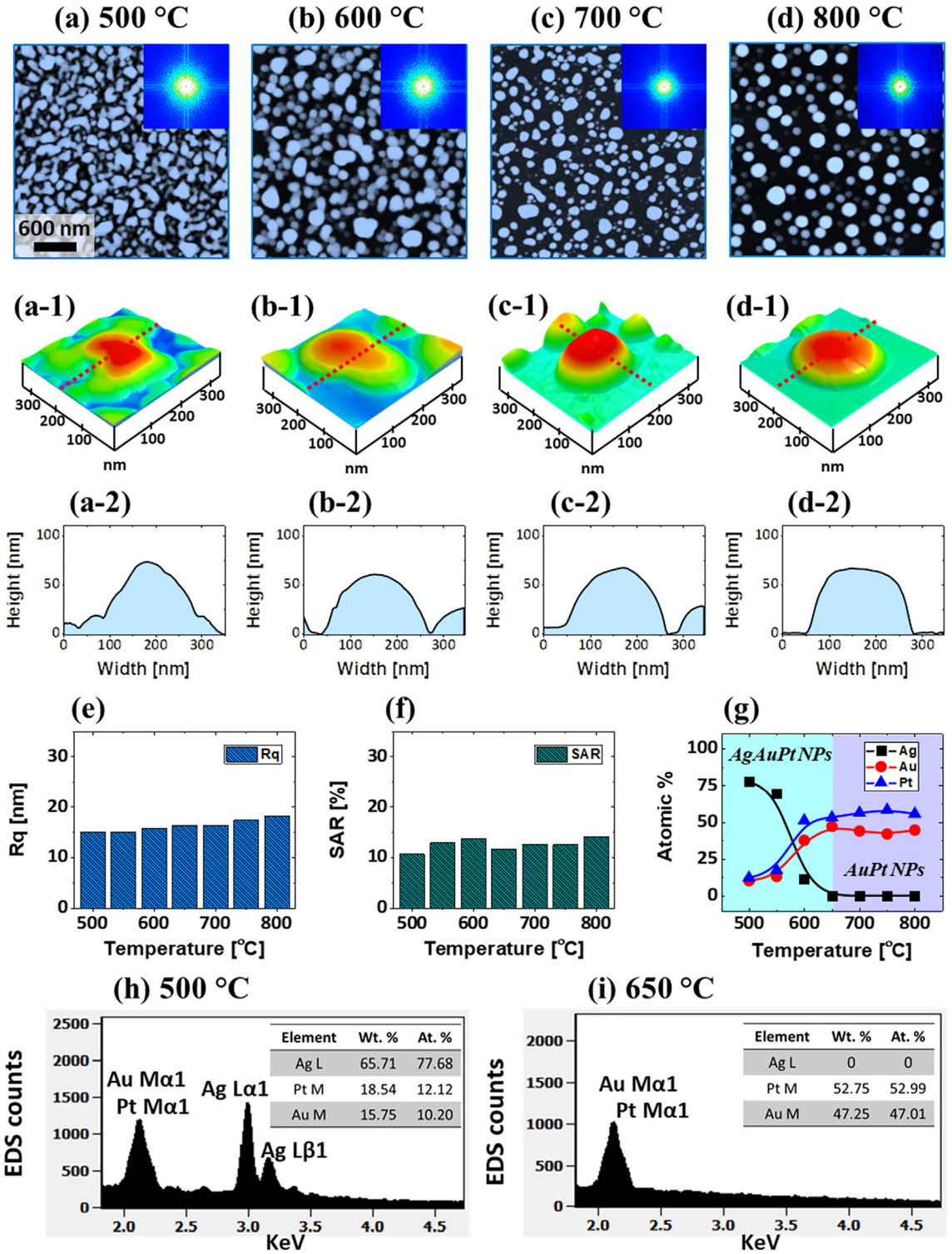

Fig. 4. Fabrication of isolated medium size AgAuPt and AuPt alloy NPs by the dewetting of $Ag_{11nm}/Au_{3nm}/Pt_{3nm}$ tri-layers based on annealing between 500 and 800 °C for 120 s. (a) – (d) AFM top-views (3 × 3 μm^2) of the alloy NPs. Insets show the Fourier filter transform (FFT) pattern of corresponding AFM images. (a-1) – (d-1) AFM side-views showing the typical alloy NPs at different temperatures. (a-2) – (d-2) Corresponding line profiles across the typical alloy nanostructures. (e) – (g) Summary plots of the Rq, SAR and atomic (at) % of Ag, Au and Pt. (h) – (i) EDS spectra of AgAuPt and AuPt alloy NPs fabricated at 500 and 650 °C.

to the increased backscattering and reduced absorption with the smaller size and Ag sublimation [48].

From the transmittance spectra of AgAuPt NPs in Fig. 5(c) and (c-1), it showed the shoulder formations at the wavelengths where the extinction peaks were observed. This can be likely due to the forward scattering with the larger AuAgPt NPs. When the relatively smaller AuPt NPs were formed the forward scattering was sharply reduced and obvious absorption dips were observed as shown in Fig. 5(c-2) [49]. By comparing with the large AuPt NPs from the previous set, the forward scattering effect was sharply decreased in this set due to the relatively smaller size of NPs. It also was observed that the visible region dips became gradually narrower as shown in Fig. 5(c-1) as the AuPt NPs

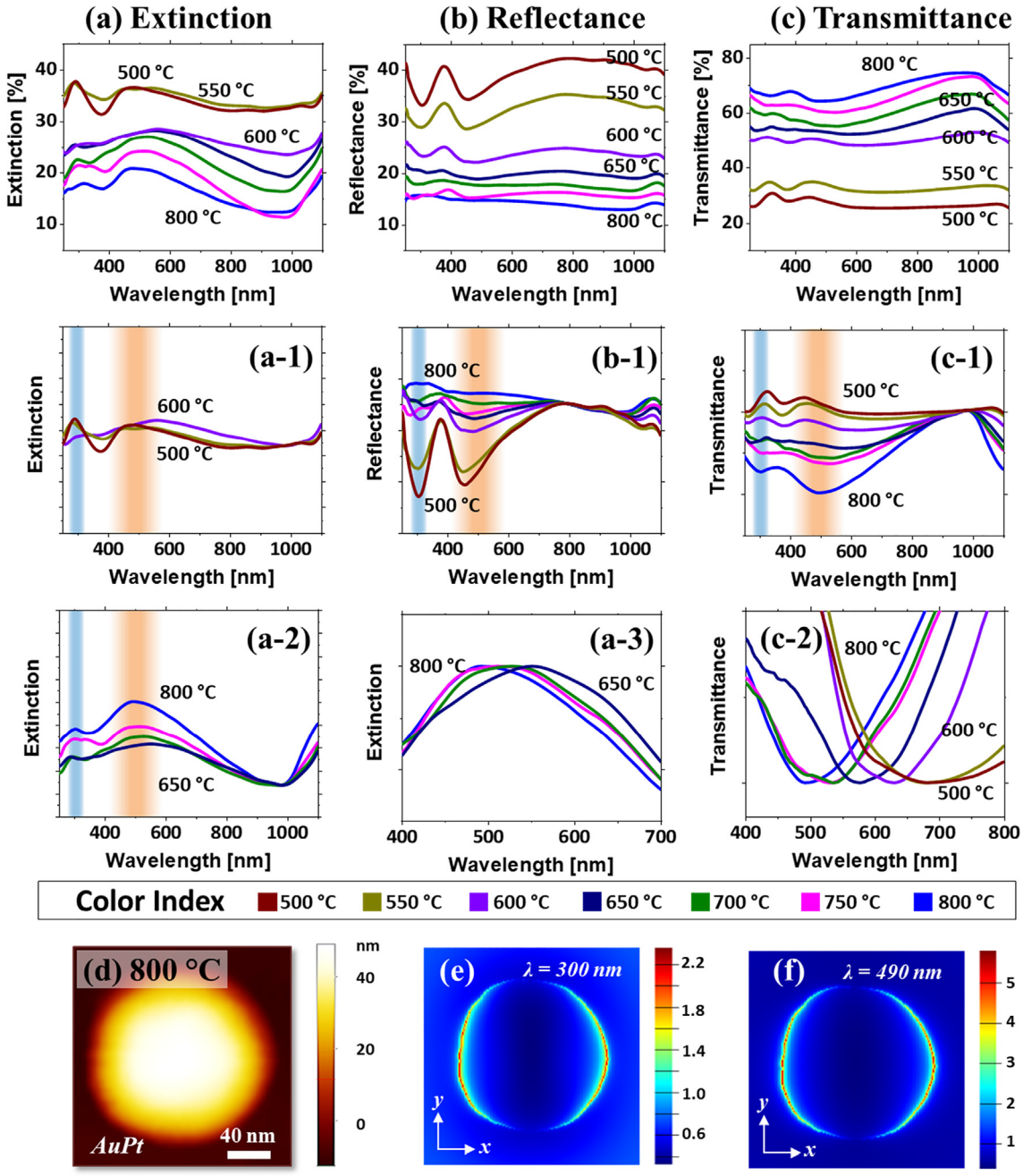

Fig. 5. Optical properties of the medium-sized AgAuPt and AuPt alloy NPs fabricated with the $Ag_{11nm}/Au_{3nm}/Pt_{3nm}$ tri-layer films. (a) – (c) Extinction, reflectance and transmittance spectra. (a-1) – (a-3) Normalized extinction spectra. (b-1) Normalized reflectance spectra. (c-1) – (c-2) Normalized transmittance spectra. (d) AFM image of the typical AuPt alloy NP selected for the FDTD analysis. (e) – (f) E-field intensity maps in x-y plane (top-view) at different wavelength as labelled.

became more uniform at the higher temperature.

Fig. 6 shows the much smaller and denser AgAuPt and AuPt alloy NPs fabricated with the $Ag_{5.5nm}/Au_{1.5nm}/Pt_{1.5nm}$ tri-layers under the identical growth condition as in the previous sets. The initial tri-layer thickness was now further reduced (8.5 nm) to realize much smaller and denser AgAuPt alloy NPs. As discussed, the dewetting extent was further accelerated with the thinner tri-layer films and resulted in the highly dense and definite NPs even at low temperatures. Small size and high areal density of NPs can be the result of rapid void perturbation and growth in the thin tri-layer films owing to the high surface diffusion and interdiffusion [51]. Furthermore, due to the lack of atoms diffusing around, the small NPs could become isolated and stable. Thus, the smaller size, semispherical configurations and larger areal density of alloy NPs were achieved in this set. As shown in Fig. 6(a) and (a-1), the tiny spherical AgAuPt NPs with the AH of ~ 9 nm and AD of ~ 46 nm were obtained at 500 °C. With the increasing temperature up to 600 °C, the NP's size was slightly reduced and the spacing between NPs was increased as observed in Fig. 6(b) and (b-1). The Rq and SAR also showed a decreasing trend as the NPs became smaller as shown in Fig. 6(e) and (f) respectively. The size reduction of NPs can be caused by the Ag sublimation as in the previous cases, which was confirmed by the EDS measurement. The at % plots in Fig. 6(g) confirmed the significant Ag sublimation happened between 500 and 600 °C such that less than 3% of Ag atoms % were detected at 600 °C and only Au and Pt were detected at higher temperature. As shown in Fig. 6(c) and (d), the average size of the NPs remained somewhat similar with the AD of ~ 40 nm and AH of ~ 9 nm at higher temperature. In addition, the Rq and SAR values also remained similar. Meanwhile, the NPs attained

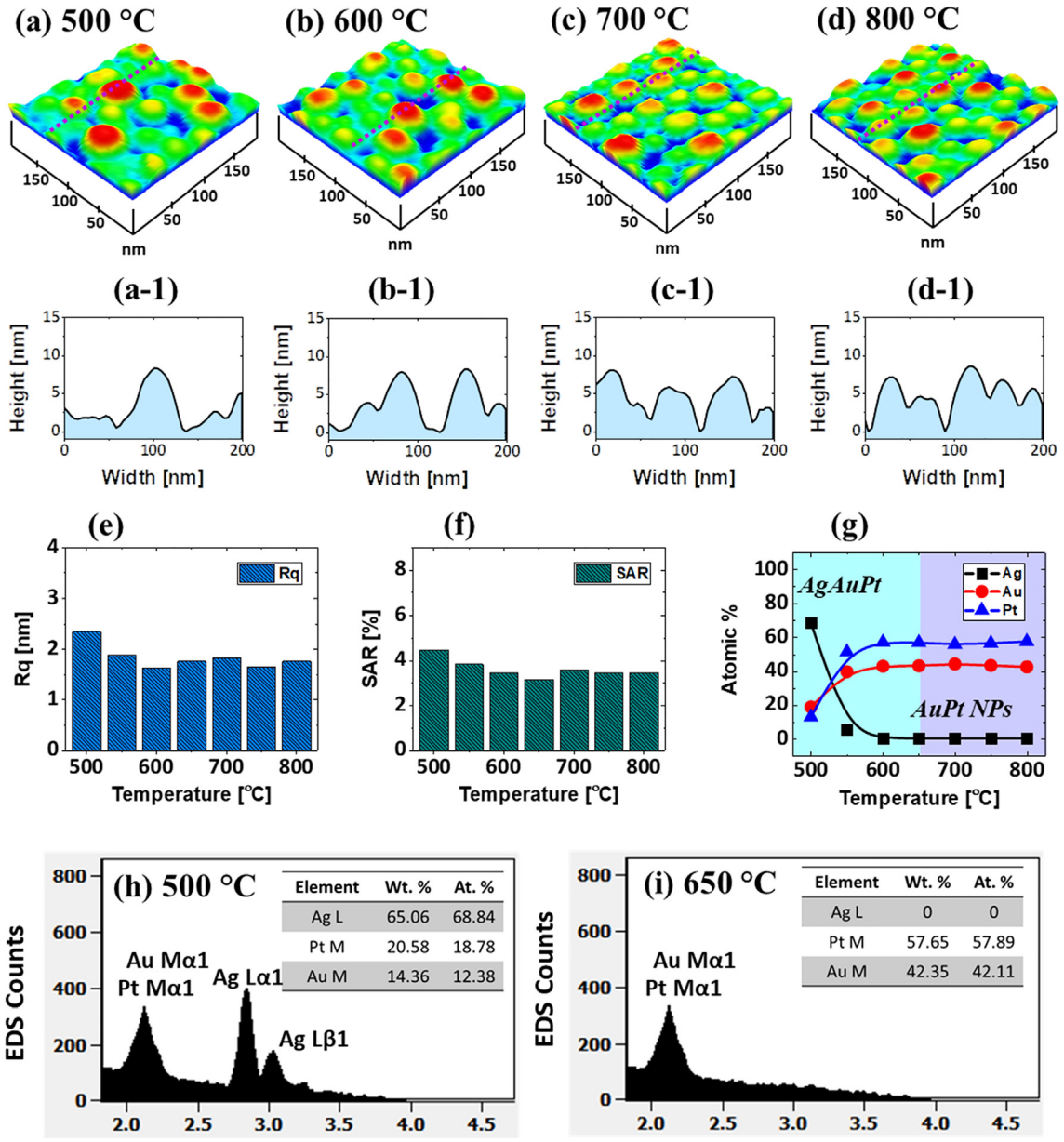

Fig. 6. Evolution of the tiny and dense AgAuPt and AuPt alloy NPs with $Ag_{5.5nm}/Au_{1.5nm}/Pt_{1.5nm}$ tri-layer annealed between 500 and 800 °C for 120 s. (a) – (d) AFM side-views (200 × 200 nm^2) of the alloy NPs. (a-1) – (d-1) Corresponding line profiles across the typical alloy NPs. (e) – (g) Summary plots of Rq, SAR and at % of Ag, Au and Pt. (h) – (i) EDS spectra of AgAuPt and AuPt alloy NPs fabricated at 500 and 650 °C. Insets show the corresponding at. % of Ag, Au and Pt.

much rounder shape with the improved uniformity due to the enhanced diffusivity of atoms with thinner films. By comparing with the previous set, the AD was reduced by four times while the AH was decreased by ten times. The detail morphological and elemental characterization of this set is provided in supplementary information in Figs. S10–S11. Furthermore, the very small AgAuPt and AuPt alloy NPs were fabricated with the $Ag_{2.2nm}/Au_{0.6nm}/Pt_{0.6nm}$ trilayer between 500 and 800 °C as shown in Figs. S13–S16, which didn't show much variation in the size and shape of NPs due to the rapid dewetting, Ag sublimation and formation of stable configurations. Generally, the tiny alloy NPs were less than 20 nm in diameter and 5 nm in height.

Fig. 7 presents the corresponding LSPR characteristics of very small and highly dense AgAuPt and AuPt alloy NPs. As compared to the previous results, the optical spectra showed clear distinctions due to the small size and high density of alloy NPs. The optical spectra were again divided based on the alloy composition of NPs: i.e. for AgAuPt and AuPt alloy NPs. In specific, the AgAuPt alloy NPs showed a strong peak in the VIS and a weaker peak in the UV region as displayed in Fig. 7(a). Since the size of alloy NPs was very small (less than50 nm) and mostly spherical in shape, the extinction peaks can be generated due to the dipolar (DR) and quadrupolar (QR) resonance modes in the VIS and UV regions [46]. The LSPR peaks of AgAuPt NPs were gradually attenuated and blue shifted at increased temperature as shown in Fig. 7(a-1), which can be correlated to the Ag sublimation as well as the size reduction. In the case of AuPt NPs, they exhibited the DR and QR bands in the VIS and UV regions respectively as shown in Fig. 7(a-2). It was also found that the DR band was slightly blue shifted as compared to the AgAuPt alloy NPs due to the smaller size of AuPt NPs [47]. The LSPR peaks of AuPt NPs was reduced between 650 and 750 °C along with the Ag sublimation and mild size reduction. The overall shift of DR peak was traced in Fig. 7(a-3), which showed a blue shift from 550 to 480 nm between 500 and 800 °C.

The e-field distribution of typical AuPt NP at 320 and 480 nm corresponding to the QR and DR respectively are presented in Fig. 7(d)–(f)

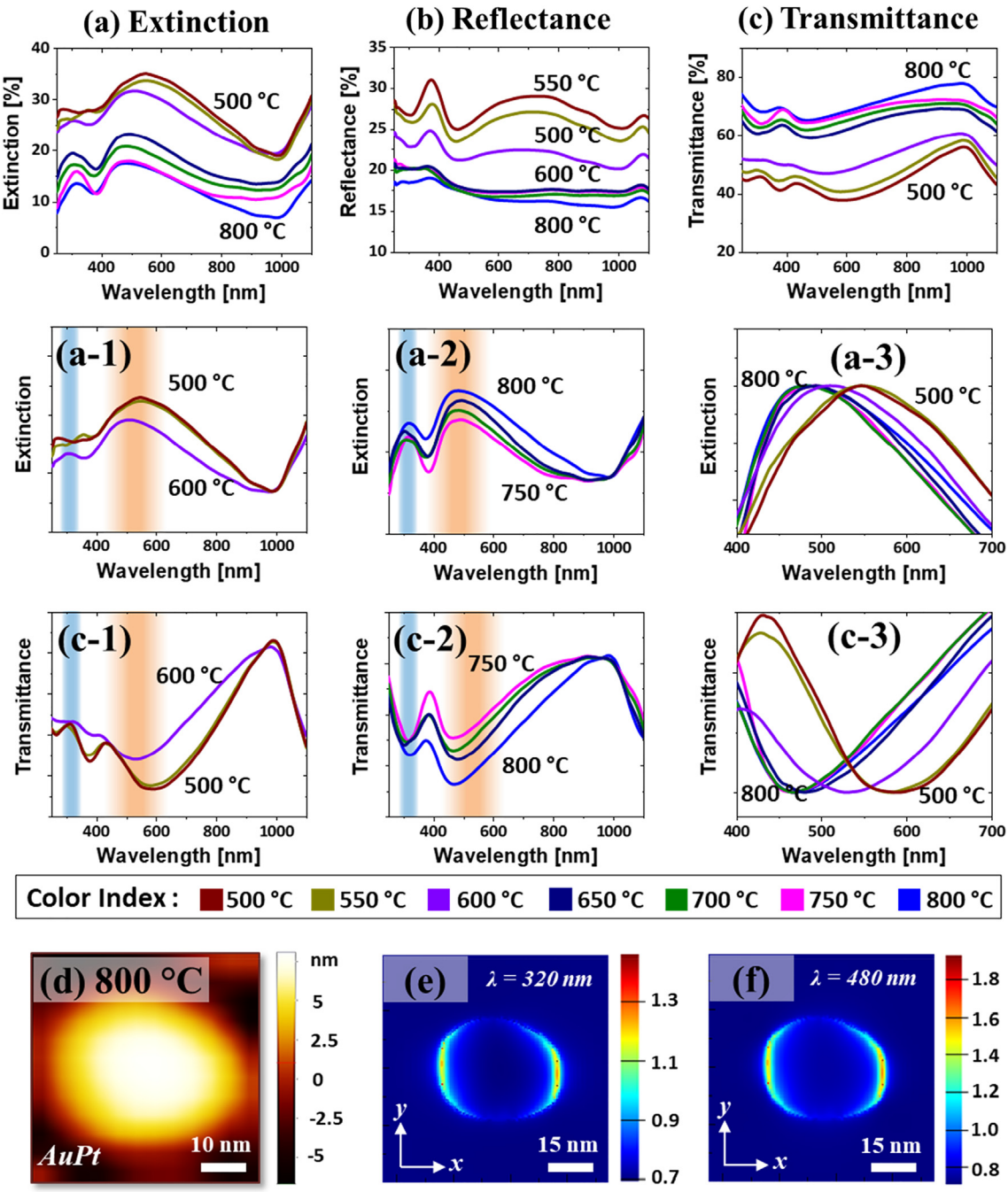

Fig. 7. LSPR properties of the tiny and dense AgAuPt and AuPt alloy NPs fabricated with the $Ag_{5.5nm}/Au_{1.5nm}/Pt_{1.5nm}$ tri-layers. (a) – (c) Extinction, reflectance and transmittance spectra of the alloy nanostructures. (a-1) – (a-3) Normalized extinction spectra. (c-1) – (c-3) Normalized transmittance spectra. (d) AFM image of the typical AuPt alloy NP chosen for the FDTD simulation. (e) – (f) E-field intensity maps in x-y plane (top-view) at different wavelength as labeled.

and Fig. S12. The overall intensity of e-field was decreased from the previous set likely due to the small size of NPs. However, the e-field was strongly confined at the boundary since the NPs were much uniform. The reflectance spectra of AgAuPt NPs in Fig. 7(b) revealed dips at ~300 and ~500 nm, which corresponds to the absorption dips due to the QR and DR modes. When the size of NPs became smaller at increased temperature, the absorption dips were reduced due to the increased backscattering along with the size reduction of NPs as well as the Ag sublimation [48]. In the case of AuPt NPs, they generally exhibited a flat behavior as the backscattering effect became more significant with the smaller size. Thus, the absorption dips were not clearly observed in the reflectance spectra. Furthermore, the transmittance spectra of AgAuPt and AuPt alloy NPs showed absorption dips in the UV and VIS region as shown in Fig. 7(c) and (c-3). The absorption dips were stronger with the AgAuPt NPs than the AuPt NPs due to the much enhanced LSPR response with the Ag content. Since the average size of NPs were reduced with temperature, the VIS transmittance dip showed a clear blue shift from 590 to 450 nm as shown in Fig. 7(c-3). In contrast to the previous large AgAuPt and AuPt NPs, the forward scattering effect was not observed in this case due to the small size of NPs.

4. Conclusions

In summary, the trimetallic AgAuPt and bimetallic AuPt alloy NPs of distinctive shape, size and density exhibiting tunable LSPR bands have been successfully demonstrated on the transparent *c*-plane sapphire

(0001). Various surface configurations of alloy NPs were demonstrated by controlling the dewetting kinetics with the annealing temperature (500 °C ≤ T ≤ 800 °C) and Ag/Au/Pt tri-layer thickness (8.5 nm ≤ n ≤ 51 nm). Besides the annealing temperature and thickness of Ag/Au/Pt tri-layer films, the Ag sublimation also showed a great impact on the surface morphology and optical response of the alloy NPs. In specific, the Ag/Au/Pt tri-layers produced AgAuPt alloy NPs below 650 °C whereas the AuPt alloy NPs were resulted at higher temperature due to the Ag sublimation. The size and areal density of the AgAuPt and AuPt were tuned by the variation of initial thickness such that larger size and reduced areal density of alloy NPs were realized with the thicker tri-layers. From the optical analysis of these alloy NPs, the strong LSPR peaks in the UV and VIS regions were revealed. In specific, the AgAuPt alloy NPs had relatively stronger peaks while the AuPt NPs showed broader and weaker LSPR bands. Depending upon the evolution of size, uniformity, structure and elemental compositions of the alloy NPs, the excitation of various LSPR modes such as dipolar, quadrupolar, multipolar and higher order modes were observed in specific wavelength.

Declaration of Competing Interest

The authors declare that they have no known competing financial interests or personal relationships that could have appeared to influence the work reported in this paper.

Acknowledgments

Financial support from the National Research Foundation of Korea (no. NRF-2019R1A2C4069438 and NRF-2018R1A6A1A03025242) and in part by the research grant of Kwangwoon University in 2019 is gratefully acknowledged. Special appreciations to Ms. So Hee Kim from the Korea Institute of Science and Technology (KIST) for the SEM-EDX characterizations. Also, the work reported in this paper was conducted during the sabbatical year of Kwangwoon University in 2019.

Appendix A. Supplementary material

Supplementary data to this article can be found online at https://doi.org/10.1016/j.apsusc.2019.144545.

References

[1] Philipp Reineck, Delia Brick, Paul Mulvaney, Udo Bach, Plasmonic hot electron solar cells: the effect of nanoparticle size on quantum efficiency, J. Phys. Chem. Lett. 7 (20) (2016) 4137–4141.
[2] Yao, Jung-Min Hwang Yung-Chi, Zu-Po Yang, Jing-Yu Haung, Chia-Ching Lin, Wei-Chen Shen, Chun-Yang Chou, et al., Enhanced external quantum efficiency in GaN-based vertical-type light-emitting diodes by localized surface plasmons, Scient. Rep. 6 (2016) 22659.
[3] Sergio Navalon, Amarajothi Dhakshinamoorthy, Mercedes Alvaro, Hermenegildo Garcia, Metal nanoparticles supported on two-dimensional graphenes as heterogeneous catalysts, Coord. Chem. Rev. 312 (2016) 99–148.
[4] Anders Kristensen, Joel KW Yang, Sergey I. Bozhevolnyi, Stephan Link, Peter Nordlander, Naomi J. Halas, N. Asger Mortensen, Plasmonic colour generation, Nat. Rev. Mater. 2 (1) (2017) 16088.
[5] Ghenadii Korotcenkov, Vladimir Brinzari, Beong K. Cho, Conductometric gas sensors based on metal oxides modified with gold nanoparticles: a review, Microchim. Acta 183 (3) (2016) 1033–1054.
[6] Hadis Daraee, Ali Eatemadi, Elham Abbasi, Sedigheh Fekri Aval, Mohammad Kouhi, Abolfazl Akbarzadeh, Application of gold nanoparticles in biomedical and drug delivery, Artif. Cells Nanomed. Biotechnol. 44 (1) (2016) 410–422.
[7] Quang Cong Tong, Mai Hoang Luong, Jacqueline Remmel, Minh Thanh Do, Dam Thuy Trang Nguyen, Ngoc Diep Lai, Rapid direct laser writing of desired plasmonic nanostructures, Opt. Lett. 42 (12) (2017) 2382–2385.
[8] Xiaolin Hu, Jian Tian, Yanjun Xue, Yujie Li, Hongzhi Cui, Bi2WO6 nanosheets decorated with Au nanorods for enhanced near-infrared photocatalytic properties based on surface plasmon resonance effects and wide-range near-infrared light harvesting, ChemCatChem 9 (8) (2017) 1511–1516.
[9] Seon Mi Yoo, Sher Bahadur Rawal, Ji Eun Lee, Jeongho Kim, Han-Youl Ryu, Dong-Wha Park, Wan In Lee, Size-dependence of plasmonic Au nanoparticles in photocatalytic behavior of Au/TiO2 and Au@ SiO2/TiO2, Appl. Catal. A 499 (2015) 47–54.
[10] Xiaotong Liu, Dabing Li, Xiaojuan Sun, Zhiming Li, Hang Song, Hong Jiang, Yiren Chen, Tunable dipole surface plasmon resonances of silver nanoparticles by cladding dielectric layers, Sci. Rep. 5 (2015) 12555.
[11] Y. Hua, K. Chandra, D.H. Dam, G.P. Wiederrecht, T.W. Odom, Shape-dependent nonlinear optical properties of anisotropic gold nanoparticles, J. Phys. Chem. Lett. 6 (24) (2015) 4904–4908.
[12] Amit Bansal, S.S. Verma, Optical response of noble metal alloy nanostructures, Phys. Lett. A 379 (3) (2015) 163–169.
[13] Chen Gong, Mariama Rebello Sousa Dias, Garrett C. Wessler, Joshua A. Taillon, Lourdes G. Salamanca-Riba, Marina S. Leite, Near-field optical properties of fully alloyed noble metal nanoparticles, Adv. Opt. Mater. 5 (1) (2017) 1600568.
[14] Hiroyasu Nishi, Tsukasa Torimoto, Tetsu Tatsuma, Wavelength-and efficiency-tunable plasmon-induced charge separation by the use of Au–Ag alloy nanoparticles, PCCP 17 (6) (2015) 4042–4046.
[15] Anna Zielińska-Jurek, Zhishun Wei, Izabela Wysocka, Piotr Szweda, Ewa Kowalska, The effect of nanoparticles size on photocatalytic and antimicrobial properties of Ag-Pt/TiO 2 photocatalysts, Appl. Surf. Sci. 353 (2015) 317–325.
[16] Ana L. Luna, Ekaterina Novoseltceva, Essyllt Louarn, Patricia Beaunier, Ewa Kowalska, Bunsho Ohtani, Miguel A. Valenzuela, Hynd Remita, Christophe Colbeau-Justin, Synergetic effect of Ni and Au nanoparticles synthesized on titania particles for efficient photocatalytic hydrogen production, Appl. Catal. B 191 (2016) 18–28.
[17] Macarena Munoz, Sebastian Ponce, Gui-Rong Zhang, Bastian JM Etzold, Size-controlled PtNi nanoparticles as highly efficient catalyst for hydrodechlorination reactions, Appl. Catal. B 192 (2016) 1–7.
[18] Sarina Sarina, Huaiyong Zhu, Esa Jaatinen, Qi Xiao, Hongwei Liu, Jianfeng Jia, Chao Chen, Jian Zhao, Enhancing catalytic performance of palladium in gold and palladium alloy nanoparticles for organic synthesis reactions through visible light irradiation at ambient temperatures, J. Am. Chem. Soc. 135 (15) (2013) 5793–5801.
[19] Tongtong Jiang, Chuancheng Jia, Lanchun Zhang, Shuren He, Yuanhua Sang, Haidong Li, Yanqing Li, Xu. Xiaohong, Hong Liu, Gold and gold–palladium alloy nanoparticles on heterostructured TiO 2 nanobelts as plasmonic photocatalysts for benzyl alcohol oxidation, Nanoscale 7 (1) (2015) 209–217.
[20] Fu-Min Li, Yong-Qiang Kang, Hui-Min Liu, Ya-Nan Zhai, Hu. Man-Cheng, Yu. Chen, Atoms diffusion-induced phase engineering of platinum-gold alloy nanocrystals with high electrocatalytic performance for the formic acid oxidation reaction, J. Colloid Interface Sci. 514 (2018) 299–305.
[21] Kontee Thongthai, Phakkhananan Pakawanit, Narong Chanlek, Jun-Hyun Kim, Supon Ananta, Laongnuan Srisombat, Ag/Au/Pt trimetallic nanoparticles with defects: preparation, characterization, and electrocatalytic activity in methanol oxidation, Nanotechnology 28 (37) (2017) 375602.
[22] E.D. Palik ed., Handbook of optical constants of solids Vol 1998 Academic press 3).
[23] D. Rakić, A.B. Djurišic, J.M. Elazar, M.L. Majewski, Optical properties of metallic films for vertical-cavity optoelectronic devices, Appl. Opt. 37 (1998) 5271–5283.
[24] D.R. Lide, CRC handbook of chemistry and physics, HandbChem. Phys. 53 (2003) 2616.
[25] Guang Yang, Fu. Xiao-Jian, Jing-Bo Sun, Ji Zhou, Spectroscopic ellipsometry study on the optical dielectric properties of silver platinum alloy thin films, J. Alloy. Compd. 551 (2013) 352–359.
[26] Minhee Kang, Myeong-Su Ahn, Youngseop Lee, Ki-Hun Jeong, Bioplasmonic alloyed nanoislands using dewetting of bilayer thin films, ACS Appl. Mater. Interfaces 9 (42) (2017) 37154–37159.
[27] Sundar Kunwar, Puran Pandey, Mao Sui, Sushil Bastola, Jihoon Lee, Evolution of ternary AuAgPd nanoparticles by the control of temperature, thickness, and tri-layer, Metals7 11 (no. 2017,) 472.
[28] Anna Kosinova, Oleg Kovalenko, Leonid Klinger, Eugen Rabkin, Mechanisms of solid-state dewetting of thin Au films in different annealing atmospheres, Acta Mater. 83 (2015) 91–101.
[29] Sundar Kunwar, Ming-Yu Li, Puran Pandey, Mao Sui, Quanzhen Zhang, Jihoon Lee, Evolution of morphological and optical properties of self-assembled Ag nanostructures on c-plane sapphire (0001) by the precise control of deposition amount, Mater. Res. Exp. 3 (12) (2016) 125006.
[30] Puran Pandey, Mao Sui, Ming-Yu Li, Quanzhen Zhang, Eun-Soo Kim, Jihoon Lee, Shape transformation of self-assembled Au nanoparticles by the systematic control of deposition amount on sapphire (0001), RSC Adv. 5 (81) (2015) 66212–66220.
[31] Mao Sui, Ming-Yu Li, Sundar Kunwar, Puran Pandey, Quanzhen Zhang, Jihoon Lee, Effects of annealing temperature and duration on the morphological and optical evolution of self-assembled Pt nanostructures on c-plane sapphire, PLoS ONE 12 (5) (2017) e0177048.
[32] Jongpil Ye, Carl V. Thompson, Anisotropic edge retraction and hole growth during solid-state dewetting of single crystal nickel thin films, Acta Mater. 59 (2) (2011) 582–589.
[33] Levente Vitos, A.V. Ruban, Hans Lomholt Skriver, J. Kollar, The surface energy of metals, Surf. Sci. 411 (1–2) (1998) 186–202.
[34] Andreas Herz, Felix Theska, Diana Rossberg, Thomas Kups, Dong Wang, Peter Schaaf, Solid-state dewetting of Au–Ni bi-layer films mediated through individual layer thickness and stacking sequence, Appl. Surf. Sci. 444 (2018) 505–510.
[35] Sundar Kunwar, Puran Pandey, Mao Sui, Sushil Bastola, Jihoon Lee, Fabrication of ternary AgPdAu alloy nanoparticles on c-plane sapphire by the systematical control of film thickness and deposition sequence, Metall. Mater. Trans. A 49 (6) (2018) 2352–2362.
[36] Yoonseok Oh, Jeeyoung Lee, Myeongkyu Lee, Fabrication of Ag-Au bimetallic nanoparticles by laser-induced dewetting of bilayer films, Appl. Surf. Sci. 434 (2018)

1293–1299.
[37] J.B. Park, S.F. Conner, D.A. Chen, Bimetallic Pt− Au clusters on TiO2 (110): growth, surface composition, and metal− support interactions, J. Phys. Chem. C 112 (14) (2008) 5490–5500.
[38] Surendra Singh, Mitali Swain, Saibal Basu, Kinetics of interface alloy phase formation at nanometer length scale in ultra-thin films: X-ray and polarized neutron reflectometry, Prog. Mater Sci. (2018).
[39] C. Manuela Müller, R. Spolenak, Dewetting of Au and AuPt alloy films: a dewetting zone model, J. Appl. Phys. 113 (9) (2013) 094301.
[40] H. Khoussa, B. Baris, M. Alchaar, F. Chaumeton, M. Ghamnia, S. Gauthier, D. Martrou, Morphology and work function of In, Ag, Mg, and Au nano-islands grown on AlN (0001) surface, Phys. Status Solidi (B) 255 (5) (2018) 1700482.
[41] S.K. Sharma, J. Spitz, Hillock formation, hole growth and agglomeration in thin silver films, Thin Solid Films 65 (3) (1980) 339–350.
[42] P. Jacquet, R. Podor, J. Ravaux, J. Lautru, J. Teisseire, I. Gozhyk, J. Jupille, R. Lazzari, On the solid-state dewetting of polycrystalline thin films: capillary versus grain growth approach, Acta Mater. (2017).
[43] Yong Ding, Fengru Fan, Zhongqun Tian, Zhong Lin Wang, Sublimation-induced shape evolution of silver cubes, Small 5 (24) (2009) 2812–2815.
[44] Donghyun Kim, Amanda L. Giermann, Carl V. Thompson, Solid-state dewetting of patterned thin films, Appl. Phys. Lett. 95 (25) (2009) 251903.
[45] H. Galinski, T. Ryll, P. Elser, J.L.M. Rupp, A. Bieberle-Hütter, L.J. Gauckler, Agglomeration of Pt thin films on dielectric substrates, Phys. Rev. B 82 (23) (2010) 235415.
[46] Kelly KL, Coronado E, Zhao LL, Schatz GC. "The optical properties of metal nanoparticles: the influence of size, shape, and dielectric environment. (2003): pp. 668–677.
[47] Jingyi Chen, Benjamin Wiley, Joseph McLellan, Yujie Xiong, Zhi-Yuan Li, Younan Xia, Optical properties of Pd− Ag and Pt− Ag nanoboxes synthesized via galvanic replacement reactions, Nano Lett. 5 (10) (2005) 2058–2062.
[48] Sh.a. Liu, Guanying Chen, Paras N. Prasad, Mark T. Swihart, Synthesis of monodisperse Au, Ag, and Au–Ag alloy nanoparticles with tunable size and surface plasmon resonance frequency, Chem. Mater. 23 (18) (2011) 4098–4101.
[49] G. Schmidl, J. Dellith, H. Schneidewind, D. Zopf, O. Stranik, A. Gawlik, S. Anders, et al., Formation and characterization of silver nanoparticles embedded in optical transparent materials for plasmonic sensor surfaces, Mater. Sci. Eng., B 193 (2015) 207–216.
[50] K. Govatsi, A. Chrissanthopoulos, V. Dracopoulos, S.N. Yannopoulos, The influence of Au film thickness and annealing conditions on the VLS-assisted growth of ZnO nanostructures, Nanotechnology 25 (21) (2014) 215601.
[51] Dong Wang, Ran Ji, Peter Schaaf, Formation of precise 2D Au particle arrays via thermally induced dewetting on pre-patterned substrates, Beilstein J. Nanotechnol. 2 (2011) 318.